Real Time Intraoperative Functional Brain Mapping Based on RGB Imaging

C. Caredda, L. Mahieu-Williame, R. Sablong, M. Sdika, J. Guyotat, B. Montcel

Version of Record: https://www.sciencedirect.com/science/article/pii/S195903182030083X
Manuscript_18b087b3615d6fe7b4ae3940c4297b82

Real time intraoperative functional brain mapping based on RGB imaging

Abstract

Intraoperative optical imaging is a localization technique for the functional areas of the human brain cortex during neurosurgical procedures. However, it still lacks robustness to be used as a clinical standard. In particular new biomarkers of brain functionality with improved sensitivity and specificity are needed. We present a method for the real time identification of the activated cortical areas based on the analysis of the cortical hemodynamic using a RGB camera and a white light source. We measure the quantitative oxy and deoxy-hemoglobin concentration changes in the human brain cortex with the modified Beer-lambert law and Monte Carlo simulations. A functional model has been implemented to define in real time a binary biomarker of the cortical activation following neuronal activation by physiological stimuli. The results show a good correlation between the computed activation maps and the brain areas localized by electrical brain stimulation. We demonstrate that a RGB camera combined with a quantitative modeling of brain hemodynamics biomarkers can evaluate in real time the functional areas during neurosurgery and serve as a tool of choice to complement electrical brain stimulation.

Keywords: functional brain mapping, real time processing, intraoperative imaging, optical imaging, RGB camera

1. INTRODUCTION

Non-invasive functional brain mapping is an imaging technique used to localize the functional areas of the patient brain. This technique is used during brain tumor resection surgery to indicate to the neurosurgeon the cortical tissues which should not be removed without cognitive impairment. Functional magnetic resonance imaging (fMRI)[1] is widely used to localize patient functional areas. However, after patient craniotomy, a brain shift invalidates the relevance of neuro-navigation to intraoperatively localize the functional areas of the patient brain[2]. In order to prevent any localization error, intraoperative MRI has been suggested but it complicates the surgery gesture which makes it rarely used. For these reasons, electrical brain stimulation (EBS)[3] is preferred during neurosurgery for the identification of brain functional areas.

In 1977, *Jöbsis*[4] demonstrated that the blood and tissue oxygenation changes in the brain can be measured using near-infrared (NIR) light. Then, *Chance et al.*[5] demonstrated that optical imaging (visible and NIR light) can monitor the brain activity with the determination of concentration changes of oxygenated hemoglobin (ΔC_{HbO_2}), deoxygenated

hemoglobin (ΔC_{Hb}), blood volume ($\Delta C_{HbO_2} + \Delta C_{Hb}$) and cytochrome oxidase. Since then, numerous works have demonstrated the ability of optical imaging to detect functional areas thanks to hemodynamics[6, 7, 8, 9, 10, 11, 12].

During neurosurgery, the craniotomy gives a direct access to the brain cortex. Intrinsic optical imaging[13, 14, 15] can be used intraoperatively to localize the patient hemodynamic activity in the cerebral cortex. The intrinsic signal refers to the cortical reflectance changes[13, 16] due to hemodynamic response. A hyperspectral camera[17, 18] or a single wavelength illumination in conjunction with a low-noise CCD camera[19, 15] can be used to acquire the intrinsic signal. The time course of this signal is characterized by the early hemodynamic responses in brain tissue related to neuronal activity (initial dip) followed by a larger response which corresponds to the blood oxygenation level-dependent (BOLD) contrast in fMRI studies[16]. This technique is a powerful tool to understand the cognitive functions at the neural circuit level[14] and to define more precisely the hemodynamic response following a physiological stimulus[20, 21]. In some studies, a spectroscopic analysis of the intrinsic signal is computed to asses the cortical hemoglobin concentration changes. New approaches consist in using a RGB[20, 22] or hyperspectral[17] camera with a continuous wave white light source[20, 17, 23] or pulsed narrow bandpass illumination sources[22, 24]. These setups have the main advantages of being usable in real time[17, 24] and directly in the operative room. *Steimers et al.*[22] analyzed an exposed rat cortex with a RGB-LED light source and a RGB camera. The results of their work indicate that semi-quantitative functional maps (in arbirary units) can be processed with the modified Beer-Lambert law. But the optical mean optical path lengths were not taken into consideration. *Bouchard et al.*[24] developed an ultra fast device made up of two pulsed LEDs and a monochromatic camera to assess in real time the hemoglobin concentration changes in blood vessels using the modified Beer-Lambert law. *Pichette et al.*[17] used a hyperspectral camera and a continuous wave white light illumination to compute a video-rate assessment of the hemoglobin concentration changes folowing a patient epilepsy seizure. In their study, the blood vessels and the grey matter pixels were automatically segmented by comparing measured reflectance spectra to blood and grey matter simulated reflectance spectra. This allowed the blood vessels to be masked to reduce their influence on absorbance change measurements. In these works, qualitative or quantitative brain maps are not compared to the patient hemodynamic response[25]. So it remains difficult for the neurosurgeon to efficiently localize the functional brain areas with a RGB camera.

We proposed in a previous study[26, 27] a functional model based on the analysis of the hemodynamics in brain tissue following the neuronal activation which are closely linked to the BOLD contrast used in functional MRI studies. The objective of the present work is to supply the methodological tools for the real time identification of the patient activated cortical areas during neurosurgery. We propose to compute a binary marker of the cortical activation based on the work established in our previous study[27]. The term "real time" means that the identification of the patient activated cortical areas is computed during the data acquisition and provided to the neurosurgeon as soon as possible. For each camera pixel, the intrinsic signal was converted into oxy- and deoxygenated hemoglobin concentration changes using the modified Beer-Lambert law. This law was computed with

an estimated mean optical path length calculated by Monte-Carlo simulations. Statistical analyses inspired by the BOLD fMRI method were implemented to define a binary biomarker of the cortical activation. The brain areas identified by intraoperative electrical stimulation showed a good correlation with the activation maps processed with the proposed method once the patient stopped the activity procedure. However, the activation maps provided during the activity step did not provide a satisfying result due to a bad estimation of the slow drift of the collected intensity. This work could help to get a robust real time system for the intraoperative brain area identification based on RGB imaging.

2. Material and methods

2.1. Experimental setup

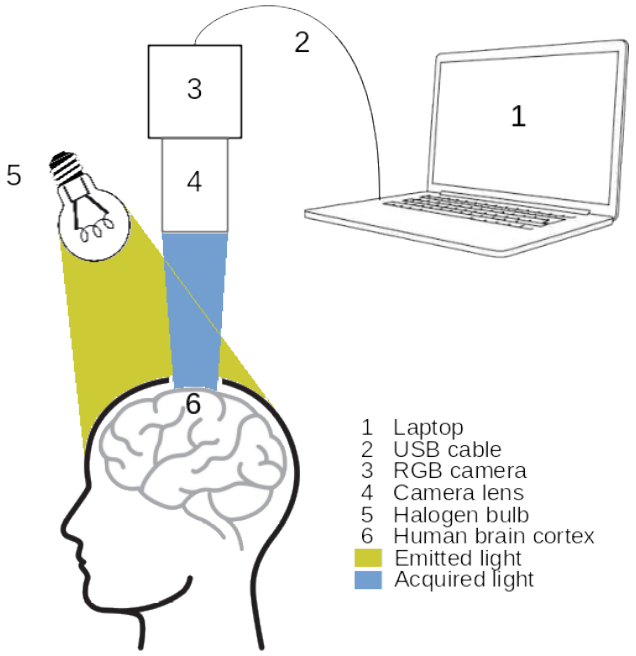

Figure 1: Schematics of the imaging system.

The imaging system is composed of a RGB CMOS camera (*BASLER acA2000-165uc*) in conjunction with an *Edmund Optics* camera lens ($f = 50mm$ $f/2 - f/22$), a continuous wave white light source (*OSRAM Classic 116W 230V* light bulb) and a laptop (processor: *Intel Core i5-7200U, 2.50GHz* $\times$ *4*, ram: 15.3GiB); see Fig. 1. During data acquisition, the camera also acquired residual light since the operative room lights were on. Data were directly acquired by the laptop via an USB link. A C++ software acquired and processed the images using open source tools such as *Qt* (*v*5.9.4), *openCV* (*v*3.2.0)[28], *Boost* (*v*1.71.0)[29] and *pylon* (*BASLER* library). 8 bits RGB images were acquired every 33 ms (the sampling rate is set to 30 frames per second) with a resolution which at best is 400ppi (the minimum size of a square pixel is $64 \times 64\mu m$).

2.2. Patient inclusion and experimental paradigm

The study was conducted at the neurologic center of the Pierre Wertheimer hospital in Bron, France. The patient had a low grade glioma close to the motor cortex associated with the right hand. The experiment was approved by the local ethics committee of Lyon University Hospitals (France). The participating patient signed written consent. The video was acquired after the patient craniotomy and before the brain tumor resection operation. During the acquisition of the video, the patient was awake and under anesthesia (awake surgery).

The stimulation of the motor cortex was achieved through successive fist clenching and relaxing. The paradigm consisted of 3 steps: 30s of rest, followed by 30s of stimulation and 30s of rest; see Fig. 2. The neurosurgeon performed electrical brain stimulation after RGB imaging to localize patient brain motor and sensory areas. This technique stimulates a neural network in the brain through the direct or indirect excitation of its cell membrane by using an electric current. A bipolar electrode (*Nimbus Medtronic neurostimulator*) was used in this study. The electrodes are $5mm$ apart. A biphasic current was used (pulsating frequency: $60Hz$, pulse width: $1ms$). The current intensity varied during the measurements. At the beginning, the current was set to $1mA$, then the current was increased up to $6mA$. Electrical brain stimulation introduces an artificial non-physiologic signal into the brain. For sensori-motor functions, electrical brain stimulation creates a "*positive*" effect which is mimicking a sensori-motor behavior. When the motor areas were electrically stimulated, the patient twitched his fingers. When the sensory areas were electrically stimulated, the patient expressed that he felt a sensation in his fingers.

2.3. Data pre-processing

Once an image was acquired, several steps were processed in parallel. First, the image was registered to compensate the brain repetitive motion. The algorithm developed by *Sdika et al.*[30, 31] was implemented to ensure that each camera pixel corresponds to the same cortical area all along data acquisition. The RGB intensities of the acquired image were then independently filtered with a low-pass IIR Bessel temporal filter[5] ($Fc = 0.05Hz$) to select the low frequencies of the light absorption which were associated with the cortical activity.

2.4. Functional model

A functional model was applied on the acquired images to compute a binary marker of the cortical activation. The functional model is based on the analysis of the ΔC_{Hb} and ΔC_{HbO_2} time courses using statistical tests inspired by BOLD fMRI analysis.

2.4.1. Data correction

The slow drift of the collected intensity due to cortical tissue desiccation during the video acquisition [23] was corrected through a linear regression subtracted to the original data.

2.4.2. Modified Beer Lambert law

The filtered and corrected intensities time courses were converted into absorbance changes:

$$\Delta A_i(t) = \log_{10}\left(\frac{R_i^0}{R_i(t)}\right), \tag{1}$$

where $R_i(t)$ is the reflectance intensity measured at time t by the camera color channel i (red, green or blue), R_i^0 is the reference reflectance intensity measured by the camera color channel i (average of the reflectance intensity over the duration of the first rest step of the experimental paradigm; see section 2.2). The modified Beer-Lambert law can be expressed as a matrix system [32]:

$$\begin{bmatrix} \Delta A_R(t) \\ \Delta A_G(t) \\ \Delta A_B(t) \end{bmatrix} = \begin{bmatrix} E_{R,Hb} & E_{R,HbO_2} \\ E_{G,Hb} & E_{G,HbO_2} \\ E_{B,Hb} & E_{B,HbO_2} \end{bmatrix} \times \begin{bmatrix} \Delta C_{Hb}(t) \\ \Delta C_{HbO_2}(t) \end{bmatrix} \tag{2}$$

with

$$E_{i,n} = \int \epsilon_n(\lambda).D_i(\lambda).S(\lambda).L(\lambda).d\lambda. \tag{3}$$

ϵ_n is the extinction coefficient of the chromophore n [33] (in $L.Mol^{-1}.cm^{-1}$). ΔC_{Hb} is the deoxygenated hemoglobin molar concentration changes (in $Mol.L^{-1}$) and ΔC_{HbO_2} the oxygenated hemoglobin molar concentration changes (in $Mol.L^{-1}$). Our model takes into consideration the receiving spectrum of the RGB camera and the emission spectrum of the light source. The spectral sensitivity of the detector i of the RGB camera is represented by $D_i(\lambda)$ and $S(\lambda)$ is the normalized intensity spectrum of the light source. $L(\lambda)$ is the wavelength dependent mean optical path length of the photons traveled in tissue. A global mean path length was applied to all camera pixels. Monte Carlo simulations[34] were implemented to estimate the light propagation in a homogeneous volume of grey matter. The hemoglobin concentration changes were obtained by matrix inversion.

2.4.3. Functional maps

For each camera pixel, the concentration changes time courses of the chromophore n were used to compute two variables of interest: r_n and $\overline{C_n}$. r_n is the Pearson correlation coefficient computed between the ΔC_n time course and the expected hemodynamic response. The expected hemodynamic response was defined as the convolution of the hemodynamic impulse response function [25] with the window function representing the experimental paradigm, see the red curve in the Fig 2. $\overline{C_n}$ is the ΔC_n value averaged over the patient activity period. A functional map was defined as the cartography of the $\overline{C_n}$ values on the region of interest (patient exposed cortex). A display threshold was implemented to display only pixels whose r_n value is higher than 0.5.

2.4.4. Activation maps

In our study, an activated cortical area is a cortical area that is associated with the patient hand stimulation; see section 2.2. The ΔC_{Hb} and ΔC_{HbO_2} time courses of an activated cortical area should be highly correlated with the expected hemodynamic response whereas the ones of an non activated cortical area should not. The $\overline{C_{Hb}}$ and $\overline{C_{HbO_2}}$ values of an activated cortical area should be significantly different from those calculated for a non activated cortical areas.

The region of interest of the patient exposed cortex was divided into N cortical areas $Cort$. Each area is defined as a group of 7×7 pixels ($1.8mm$ wide squares). Among these N cortical areas, an area which was defined as non activated by the electrical brain stimulation was selected as a reference area Ref. Successive Welch's T-tests were computed to score the differences between the mean values of the reference area Ref ($< \overline{C_n} >_{Ref}$ and $< r_n >_{Ref}$) and those of the other cortical areas ($< \overline{C_n} >_{Cort}$ and $< r_n >_{Cort}$). The notation $< X >_{Cort}$ corresponds to the mean value of X averaged over the surface of the $Cort$ area. $\sigma(X)_{Cort}$ is the standard deviation value of X over the surface of the $Cort$ area and $\Delta(X)_{Cort}$ represents the dispersion of the X values around $< X >_{Cort}$ which is equal to $2\sigma(X)_{Cort}$.

Each $Cort$ area were tested with the H_0, H_1 and H_2 hypothesis at $1/(N-1)\%$ significance level (Bonferroni correction); see Eqs. (4), (5) and (6).

$$H_0(x) = \begin{cases} \text{True}, & \text{if } x_{Cort} \neq x_{Ref} \\ \text{False}, & \text{otherwise.} \end{cases} \tag{4}$$

$$H_1(x) = \begin{cases} \text{True}, & \text{if } x_{Cort} > x_{Ref} \\ \text{False}, & \text{otherwise.} \end{cases} \tag{5}$$

$$H_2(x) = \begin{cases} \text{True}, & \text{if } x_{Cort} < x_{Ref} \\ \text{False}, & \text{otherwise.} \end{cases} \tag{6}$$

The cortical area $Cort$ was defined as activated if the following condition was respected:

$$Cort = \begin{cases} \text{Activated}, & \text{if } H_0(< \overline{C_{Hb}} >) \,\&\, H_0(< \overline{C_{HbO_2}} >) \,\&\, H_1(< r_{HbO_2} >) \,\&\, H_2(< r_{Hb} >) \\ \text{Non activated}, & \text{otherwise.} \end{cases} \tag{7}$$

2.5. Real time processing

The pre-processing steps (see section 2.3) and the functional model (see section 2.4) were implemented in a real-time architecture; see Fig. 2. In our application, the term real time means that the binary biomarker of the cortical activation was computed during the data acquisition, a few seconds after the start of the patient physiological activity. Indeed, following the neuronal activation, a slow oxygenation change occurs in the activated area. An activation map cannot be computed for each new acquired image but few seconds after the start of the patient physiological stimulus. The pre-processing steps (see section 2.3)

and the model (see section 2.4) were executed in different parallel threads. For each new acquired image (thread 1 in red), the brain motion was compensated (thread 2 in blue). Then, the RGB intensities of the acquired image were independently filtered (thread 3 in green). Once the cortical activation started, the activation maps A_k ($k \in [1; K]$) were recursively computed until the end of the acquisition (thread 4 in black). An intermediate buffer was placed between each computational step allowing the data storage. These buffers were required in our real-time architecture since the processing times were different for each computational step.

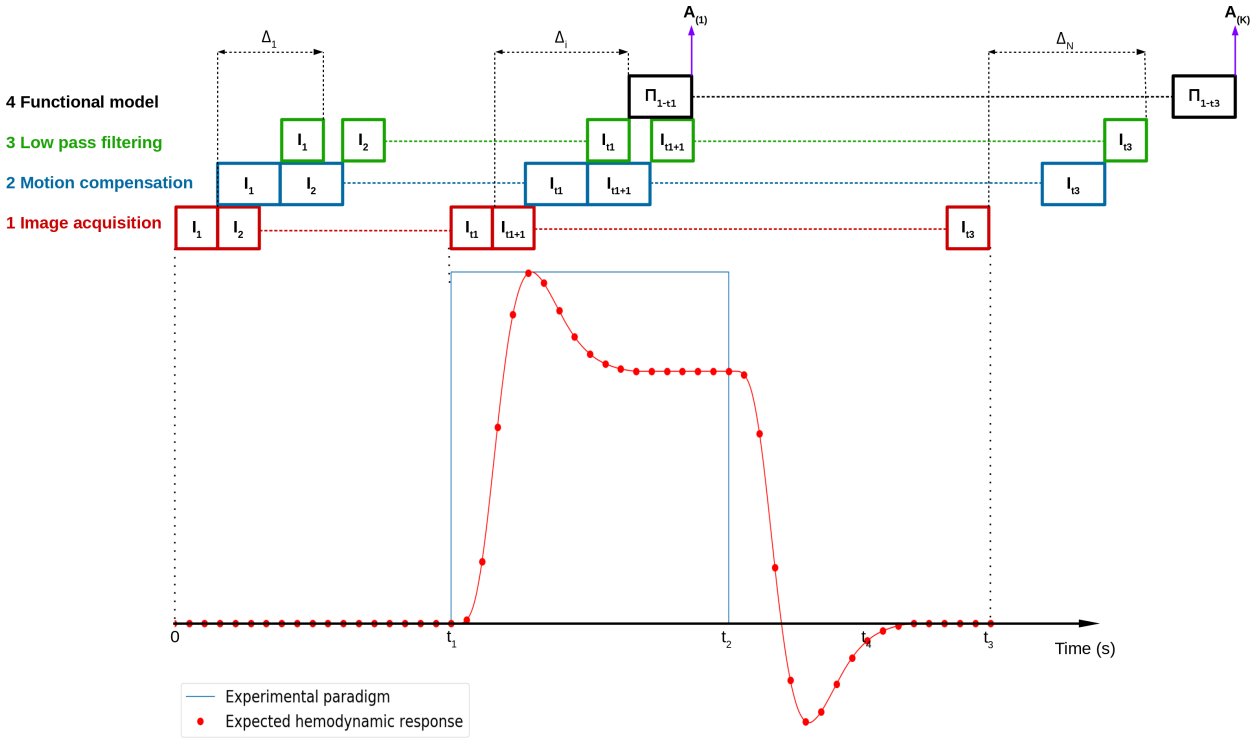

Figure 2: Overview of the real time processing. The numbers from 1 to 4 designate the four threads which are executed in parallel. For each new acquired image (thread 1 in red), the brain motion was compensated (thread 2 in blue). Then, the RGB intensities of the acquired image were independently filtered (thread 3 in green). Once the cortical activation started, the activation maps A_k ($k \in [1; K]$) were recursively computed until the end of the acquisition (thread 4 in black). The rectangle length represents a thread computation time (the representation is not to scale). The colored rectangles with the notation I_i represents the computation of the image i by the one the threads. The black rectangle with the notation Π_{1-i} denotes the application of the functional model from the image 1 to the image i. Δ_i is the computational delay of the pre-processing steps. At the bottom of the figure, the experimental paradigm (see section 2.2) and the expected hemodynamic response (see section 2.4.3) are represented.

The thread corresponding to the functional model (thread 4 in black) was computed as soon as the cortical activity started ($t > t_1$; see Fig. 2). This thread was recursively called while images were pre-processed. Let consider that the image I_j is filtered, with $j \in]t_1; t_3]$; see Fig. 2. The r_n values were calculated from the ΔC_n and the expected hemodynamic

response time courses computed from the image I_1 to the image I_j. If $j < t_2$ (see Fig. 2), the $\overline{C_n}$ values were computed between the time $t = t_1$ to $t = j$. Otherwise, the $\overline{C_n}$ values were computed between the time $t = t_1$ to $t = t_2$. In the Fig. 2, a delay is represented as a free space between the low pass filtering of the image I_N and the computation of the functional map A_K. Indeed, during this delay, the computation of the functional map A_{K-1} is being processed.

3. Results

In Fig. 3, the $\overline{C_{Hb\,k}}$ and $\overline{C_{HbO_2\,k}}$ functional maps and the activation maps A_k computed in real time are represented. The $\overline{C_{Hb\,k}}$ and $\overline{C_{HbO_2\,k}}$ functional maps are plotted with a correlation threshold set to 0.3. For the $\overline{C_{HbO_2\,k}}$ functional maps, it means that only pixels whose r_{HbO_2} values are greater than 0.3 are represented. For the $\overline{C_{Hb\,k}}$ functional maps, only the pixels whose r_{Hb} values are lower than -0.3 are represented. The colorbar plotted next to the functional maps represents the scale of variation of the $\overline{C_{Hb}}$ and $\overline{C_{HbO_2}}$ values in $\mu Mol.L^{-1}$. The markers M_i and S_i designate the motor and the sensory area i which have been validated by the neurosurgeon by electrical brain stimulation. In the activation maps A_k, the blue square (group of 7×7 pixels) is a non activated cortical area defined as the cortical area of reference; see section 2.4.4. The red squares (group of 7×7 pixels) represent the activated cortical areas and the green squares (group of 7×7 pixels) the non activated cortical areas. Under the functional and activation maps, the experimental paradigm is represented. The vertical arrows indicate the display time of the functional and activation maps k. The double horizontal arrows represent the computation time of the functional and activation map k. The length of these horizontal arrows increases with the accumulation of the data and reduces at the end of the acquisition.

The functional and activation map 1 was not computed as soon as the activation started but $8s$ after the start of the patient activity. This corresponds to the delay introduced by the IIR Bessel filter. In the functional maps 1, no $\overline{C_n}$ values were displayed and all cortical areas were defined as non activated (n is either HbO_2 or Hb). Indeed, the last pre-processed frame computed in the functional thread corresponded to the start of the activation step. In the functional maps from 2 to 5, the $\overline{C_n}$ values were displayed at the level of the large blood vessel surrounding the motor and sensory areas and at the level of the large blood vessel located on the right side of the image. In the activation maps from 2 to 5, all cortical areas were defined as non activated. In the functional maps from 6 and 7, the $\overline{C_n}$ values were displayed at the level of the motor and sensory areas and at the level of the large blood vessel located on the right side of the image. In the activation maps from 6 and 7, the cortical areas were also defined as activated at these same locations.

The ΔC_{HbO_2} and ΔC_{Hb} time courses measured at the center of the S_2 area and at the center of the reference area (blue square in the activation maps of the Fig. 3) are represented in the Fig. 4. For each graph, seven concentration changes time courses are plotted. Each time course k were computed during the execution of the activation or functional maps k with $k \in [1; 7]$; see Fig. 3.

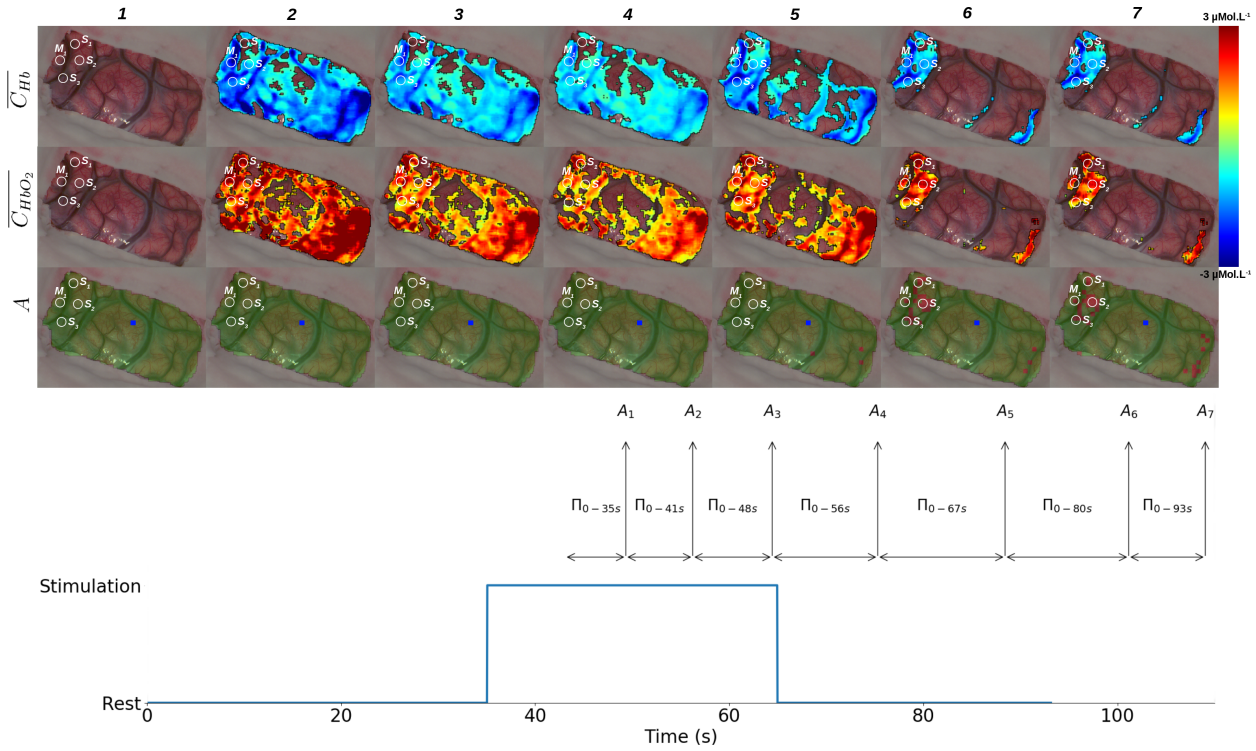

Figure 3: Functional and activation maps emitted during the video acquisition. For the $\overline{C_{Hb}}_k$ and $\overline{C_{HbO_2}}_k$ functional maps (see section 2.4.3), the correlation threshold is set to 0.3. The markers M_i and S_i designate the motor and the sensory area i which have been validated by the neurosurgeon by electrical brain stimulation. The point A is a point of interest. The colorbar represents the scale of variation of the $\overline{C_{Hb}}$ and $\overline{C_{HbO_2}}$ values in $\mu Mol.L^{-1}$. The experimental paradigm is represented in blue. The vertical arrows represent the display time of the computed functional and activation maps k and the double horizontal arrows, the computation time of these maps.

In the Fig. 4, the ranges of variation of the ΔC_{HbO_2} and ΔC_{Hb} values measured at the center of the S_2 area are 4 times greater than those measured at the center of the reference area. The range of variation of the ΔC_{HbO_2} values is 3.5 times grater than those of the ΔC_{Hb} values. The ΔC_{HbO_2} time courses measured at the center of the S_2 area seem to be positively correlated with the expected hemodynamic response while the ΔC_{HbO_2} time courses measured at the center of the reference area have a more erratic behaviour. The ΔC_{Hb} time courses measured at the center of the S_2 area seem to be negatively correlated with the expected hemodynamic response while the ΔC_{Hb} time courses measured at the center of the reference area have a more erratic behaviour. The shape of the ΔC_{HbO_2} and ΔC_{Hb} time courses from 1 to 7 differ due to the recursive execution of the data correction step; see section 2.4.1.

In the Fig. 5, the $< \overline{C_n} >$ and $< r_n >$ values (see section 2.4.4) computed for the S_2 and reference areas are plotted in solid lines (n is either HbO_2 or Hb). The $\Delta(r_n)$ and $\Delta(\overline{C_n})$ values (see section 2.4.4) computed for the S_2 and reference areas are represented with a

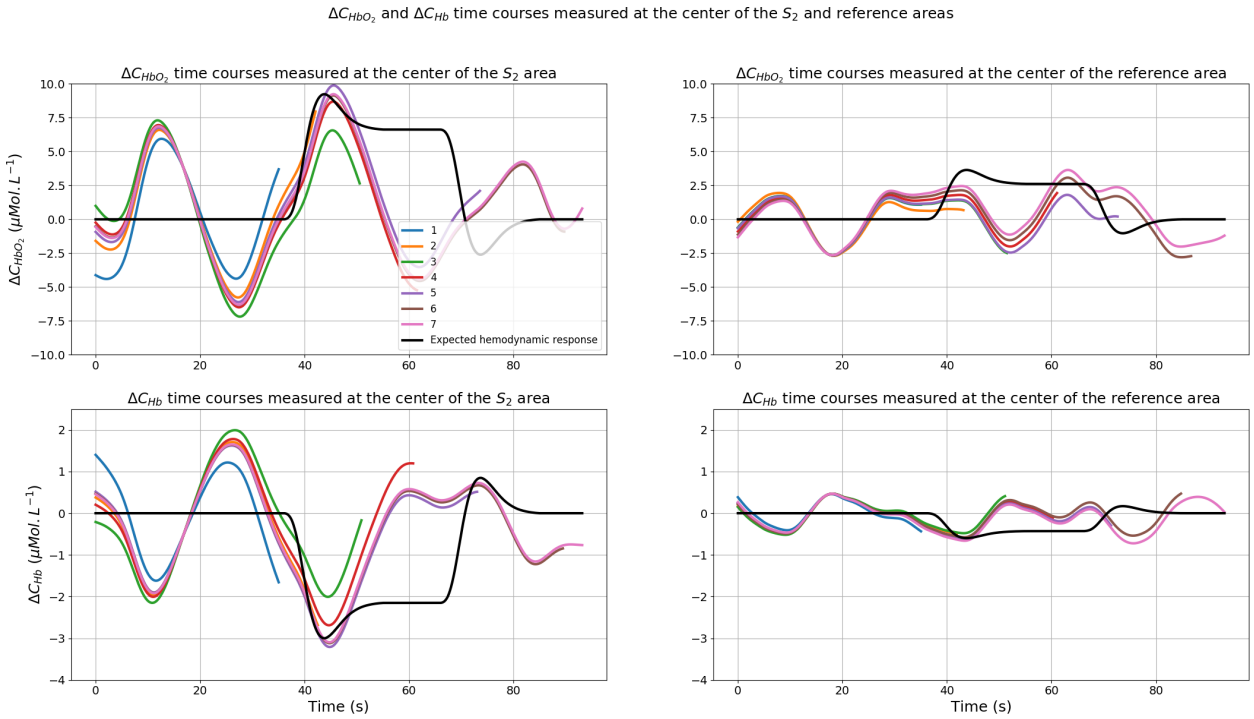

Figure 4: ΔC_{HbO_2} and ΔC_{Hb} time courses i measured at the center of the S_2 area and at the center of the reference area (blue square in the activation maps of the Fig. 3). i denotes the computation index of the functional model. The expected hemodynamic response is represented in black.

colored fill. The notation * indicates the acceptance of the statistical hypothesis used for the computation of the activation maps; see Eqs. (4), (5) and (6). These variables were calculated during the recursive execution of the functional model; see Fig. 3. Thus, the number of variable represented is equal to seven (seven activation and functional maps were processed; see Fig. 3). The temporal axes in the Fig. 5 correspond to the time index of the concentration changes time courses plotted in the Fig. 4 and do not correspond to the acquisition or display time which are represented in the Fig. 3.

In the Fig. 5, the $< \overline{C_{HbO_2}} >$ and $< \overline{C_{Hb}} >$ values of the two points of interest are equal to $0\mu Mol.L^{-1}$ from $t = 0s$ to $t = 35s$. The $< \overline{C_{HbO_2}} >$ values of the center of the S_2 area increase from $t = 35s$ (start of the activity step) to $t = 93s$ to reach a value of $2.67\mu Mol.L^{-1}$. There is, however, a decrease in values between $t = 42s$ and $t = 56s$. The $< \overline{C_{HbO_2}} >$ values of the center of the reference area fluctuate around $0\mu Mol.L^{-1}$ from $t = 35s$ to $t = 67s$. Then, from $t = 67s$ to $t = 93s$, the values decrease to $-0.50\mu Mol.L^{-1}$. The $\Delta(\overline{C_{HbO_2}})$ values of the S_2 and reference areas are equal to $0\mu Mol.L^{-1}$ from $t = 0s$ to $t = 35s$. The maximum $\Delta(\overline{C_{HbO_2}})$ value of the S_2 area is measured at $t = 41s$ with a value of $5.10\mu Mol.L^{-1}$. Then, from $t = 42s$ to $t = 93s$, the values fluctuate between 2.75 and $4.03\mu Mol.L^{-1}$. The maximum $\Delta(\overline{C_{HbO_2}})$ value of the reference area is measured at $t = 41s$ with a value of $4.74\mu Mol.L^{-1}$. Then, from $t = 42s$ to $t = 93s$, the values fluctuate between 1.99 and $3.11\mu Mol.L^{-1}$. The $\Delta(\overline{C_{HbO_2}})$ values of the S_2 and reference areas overlap from

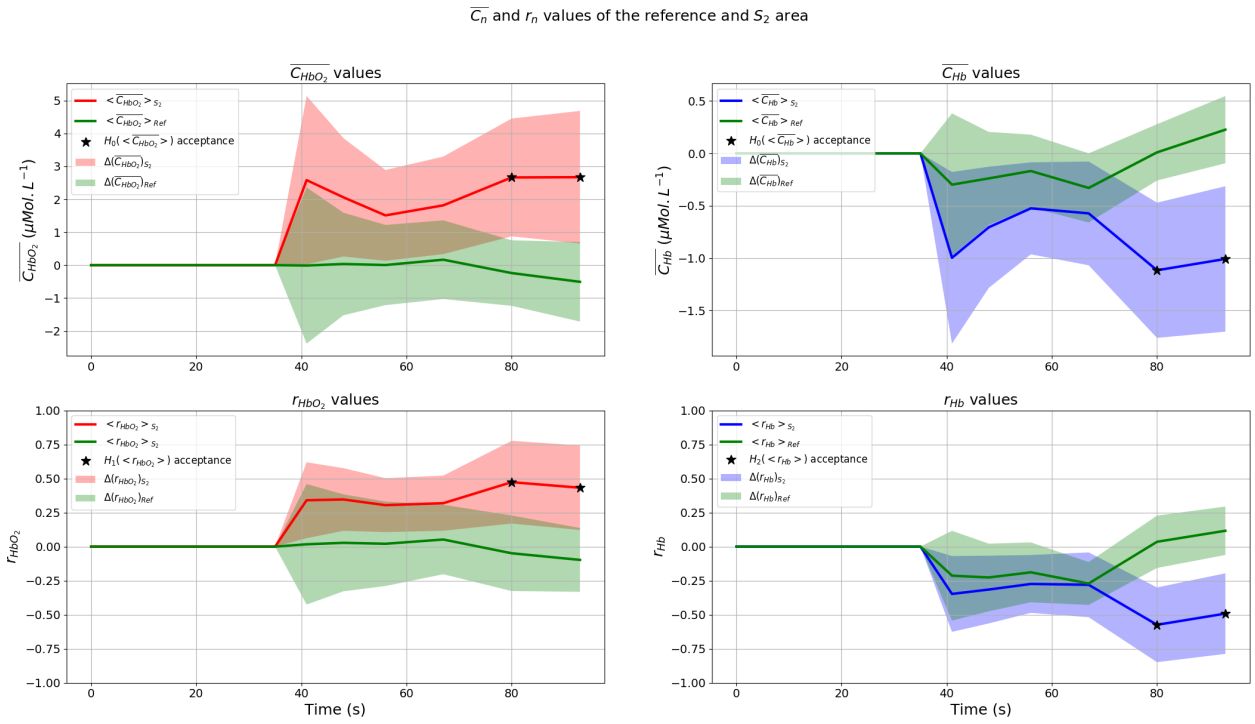

Figure 5: $< \overline{C_n} >$, $< r_n >$, $\Delta(\overline{C_n})$ and $\Delta(r_n)$ values of the S_2 and reference areas (n is either HbO_2 or Hb). The acceptance of the statistical hypotheses used in the calculation of the activation maps are represented by the marker *; see Eqs. (4), (5) and (6).

$t = 35s$ to $t = 80s$. The H_0 hypothesis is rejected for this time period. It means that there is no significant differences between the $< \overline{C_{HbO_2}} >$ values of the S_2 and reference areas. The H_0 hypothesis is accepted for the calculation of the two last activation maps.

The $< \overline{C_{Hb}} >$ values of the center of the S_2 area decrease from $t = 35s$ to $t = 93s$ to reach a value of $-1\mu Mol.L^{-1}$. There is, however, a increase in values between $t = 41s$ and $t = 56s$. The $< \overline{C_{Hb}} >$ values of the center of the reference area fluctuate around $-0.20\mu Mol.L^{-1}$ from $t = 35s$ to $t = 67s$. Then, from $t = 67s$ to $t = 93s$, the values increase to $0.23\mu Mol.L^{-1}$. The $\Delta(\overline{C_{Hb}})$ values of the S_2 and reference areas are equal to $0\mu Mol.L^{-1}$ from $t = 0s$ to $t = 35s$. The maximum $\Delta(\overline{C_{Hb}})$ value of the S_2 area is measured at $t = 41s$ with a value of $1.63\mu Mol.L^{-1}$. Then, from $t = 41s$ to $t = 93s$, the values fluctuate between 0.87 and $1.28\mu Mol.L^{-1}$. The maximum $\Delta(\overline{C_{Hb}})$ value of the reference area is measured at $t = 41s$ with a value of $1.35\mu Mol.L^{-1}$. Then, from $t = 41s$ tot $t = 93s$, the values fluctuate between 0.53 and $0.88\mu Mol.L^{-1}$. The $\Delta(\overline{C_{Hb}})$ values of the S_2 and reference areas overlap from $t = 35s$ to $t = 80s$. The H_0 hypothesis is rejected for this time period. It means that there is no significant differences between the $< \overline{C_{Hb}} >$ values of the S_2 and reference areas. The H_0 hypothesis is accepted for the calculation of the two last activation maps.

The $< r_{HbO_2} >$ and $< r_{Hb} >$ values of the two points of interest are equal to 0 from $t = 0s$ to $t = 35s$. The $< r_{HbO_2} >$ values of the center of the S_2 area increase from $t = 35s$ to $t = 93s$ to reach a value of 0.43. There is, however, a slight decrease in values between

$t = 48s$ and $t = 56s$. The $< r_{HbO_2} >$ values of the center of the reference area increase from $t = 35s$ to $t = 67s$ to reach a value of 0.05. Then, from $t = 67s$ to $t = 93s$, the values decrease to -0.09. The $\Delta(r_{HbO_2})$ values of the S_2 and reference areas are equal to $0\mu Mol.L^{-1}$ from $t = 0s$ to $t = 35s$. From $t = 35s$ to $t = 93s$, the $\Delta(r_{HbO_2})$ values of the S_2 area fluctuate between 0.39 and 0.69. The maximum $\Delta(r_{HbO_2})$ value of the reference area is measured at $t = 41s$ with a value of 0.88. Then, from $t = 41s$ to $t = 93s$, the values decrease to 0.46. The $\Delta(r_{HbO_2})$ values of the S_2 and reference areas overlap from $t = 35s$ to $t = 80s$. The H_1 hypothesis is rejected for this time period. It means that the $< r_{HbO_2} >$ values of the S_2 area are not significantly greater than the ones of the reference area. The H_1 hypothesis is accepted for the calculation of the two last activation maps.

The $< r_{Hb} >$ values of the center of the S_2 area decrease from $t = 35s$ to $t = 93s$ to reach a value of -0.49. There is, however, a slight increase in values between $t = 41s$ and $t = 67s$. The $< r_{Hb} >$ values of the center of the reference area decrease from $t = 35s$ to $t = 67s$ to reach a value of -0.27. Then, from $t = 67s$ to $t = 93s$, the values increase to 0.10. The $\Delta(r_{Hb})$ values of the S_2 and reference areas are equal to $0\mu Mol.L^{-1}$ from $t = 0s$ to $t = 35s$. From $t = 35s$ to $t = 93s$, the $\Delta(r_{Hb})$ values of the S_2 area fluctuate between 0.42 and 0.59. The maximum $\Delta(r_{Hb})$ value of the reference area is measured at $t = 41s$ with a value of 0.65. Then, from $t = 41s$ to $t = 93s$ the values decrease to 0.35. The $\Delta(r_{Hb})$ values of the S_2 and reference areas overlap from $t = 35s$ to $t = 80s$. The H_2 hypothesis is rejected for this time period. It means that the $< r_{Hb} >$ values of the S_2 area are not significantly lower than the ones of the reference area. The H_2 hypothesis is accepted for the calculation of the two last activation maps.

4. Discussion

In the Fig. 3, the cortical areas defined as activated by our method match with the motor and sensory areas identified by electrical brain stimulation. The correspondence is really effective for the activation maps A_6 and A_7 (at least $36s$ after the end of patient activity; see Fig. 3). The computation of the activation maps seems to be more robust than the computation of the $\overline{C_{HbO_2}}$ and $\overline{C_{Hb}}$ functional maps. Indeed, unlike the functional maps, no non functional areas were defined as activated during the computation of the activation maps from A_1 to A_4. Some non functional areas were still defined as activated in the activation map A_5 at the level of the large blood vessel in the middle and right side of the image. Our method can easily be implemented with standard surgical microscopes [17] and could be a useful tool for the neurosurgeon during neurosurgery.

These results should be taken with caution because our functional model needs to be improved. In particular, a physiological a priori on the hemoglobin concentration changes values could be incorporated in the model. However, there is still no consensus in the literature on such threshold values linked with a physiological stimulus. Our functional model has to be used with the electrical brain stimulation. Indeed, it requires a reference cortical area which is defined as a non functional area by the electrical brain stimulation. The main limits are that the results of the statistical analysis depend of the choice of the reference area. Moreover, the definition of the cortical activation is not obtained for each

camera pixel but computed for a group of pixels. A more robust definition of cortical areas will be explored in future works, notably with the implementation of a *SPM*[35] like analysis.

The first consistent activation map was obtained $36s$ after the end of the patient activity (see the activation map A_6 in the Fig. 3). For the functional and activation maps 1 to 5, it could be observed in the Fig. 5 that the statistical hypotheses H_0, H_1 and H_2 (see Eq. (4), (5) and (6)) were not accepted due to the overlapping of the $\Delta(\overline{C_n})$ and $\Delta(r_n)$ values between the reference and all other areas (see section 2.4.4). This can also be observed on the $\overline{C_{HbO_2}}$ and $\overline{C_{Hb}}$ functional maps from 1 to 5 in the Fig. 3 in which the concentration changes time courses measured at the level of the functional and non functional areas were both correlated with the expected hemodynamic response. For the activation map A_1, the last frame processed by the functional model corresponded to the first frame acquired during the patient activity period. This explains why no cortical areas were defined as activated. The last frames computed in the activation maps from A_2 to A_4 were acquired during the patient activity period. This may lead to an incorrect estimate of the slope of the collected intensity. Indeed, the reflectance changes associated with the cortical activation were greater than the ones caused by the tissue dessication; see section 2.4.1. This bad data correction combined with the non-consideration of the points acquired after the patient activity period lead to a bad estimate of the $\overline{C_n}$ and r_n values. For the activation map A_5, the last frame processed by the functional model was acquired $2s$ after the end of the patient activity. This $2s$ time delay was not enough to retrieve the concentration changes stability associated with the final rest step of the patient and thus could not lead to the acceptance of the statistical hypotheses of the functional model; see Figs. 3 and 5. The time delay between the start of the patient activity and the display of the first consistent activation map could be reduced by processing a calibration step before the data acquisition to learn the slope of the collected intensity. This could also reduce the computation time of the functional model.

In the Fig. 3, it can be observed that the computation time of the functional and activation maps increases with the data accumulation. This is due to the data accumulation during the acquisition and the hardware limitation inherent to our experimental setup. The computation time reduced at the end of the acquisition since the threads 1, 2 and 3 (see Fig. 2) were no longer executed. The four threads of our model (see Fig. 2) were executed in parallel by the four cores of our laptop (see section 2.1). The acquisition of the images were not perturbed by an other task in order to acquire images at 30 frames per second. However the other threads might be temporarily paused to allow the parallel execution of loops using the openMP framework (pixel-wise assessment of the hemoglobin concentration changes for instance). In addition of these parallel computing constraints, the computation time of the pre-processing steps depended on the image definition. In our application, the image were undersampled to ensure a processing time of the image registration (thread 2) and data filtering (thread 3) lower than $33ms$. The processing time of the functional model depended on the image definition and the number of processed frames. It was included between $6s$ and $13s$. A more efficient CPU (more cores) could help to fix the computation time of the threads 2 and 3 without image undersampling. It would also allow a more efficient distribution of the pixel-wise operations executed in the functional model which would lead to a faster computation of the functional and activation maps.

A global mean path length is used for each camera pixels in the modified Beer Lambert law. Monte Carlo simulations[34] were implemented to estimate the light propagation in a homogeneous volume of grey matter. Inhomogeneities of the optical properties were not taken into consideration in this study. A semi automated segmentation and a path length attribution described in our previous work[36] can help to limit the quantification error. However a lot of Monte Carlo simulations is required to model the light propagation in a volume of grey matter perfused by blood vessels of multiple diameter (from the capillaries to the arteries) to significantly reduce the partial volume effect.

5. Conclusion

In conclusion, a RGB camera and a continuous wave white light illumination seem to be a suitable setup to intraoperatively monitor the sensory and motor areas of the patient brain in real time. These results indicate that our setup could complement the actual intraoperative gold standard for the localization of patient functional areas.

Disclosures

No conflicts of interest, financial or otherwise, are declared by the authors.

Acknowledgments

This work was supported by the LABEX PRIMES (ANR-11-LABX-0063) of Université de Lyon, within the program Investissements dAvenir (ANR- 11-IDEX-0007) operated by the French National Research Agency, France Life Imaging (ANR-11-INBS-0006) and the SFGBM (BioMedical Engineering French Society / Société française de génie biologique médical). We also want to acknowledge the PILoT facility for the support provided on the image acquisition.

References

[1] S. Ogawa, T. M. Lee, A. R. Kay, D. W. Tank, Brain magnetic resonance imaging with contrast dependent on blood oxygenation., Proceedings of the National Academy of Sciences 87 (24) (1990) 9868–9872. doi:10.1073/pnas.87.24.9868.
URL http://www.pnas.org/cgi/doi/10.1073/pnas.87.24.9868

[2] I. J. Gerard, M. Kersten-Oertel, K. Petrecca, D. Sirhan, J. A. Hall, D. L. Collins, Brain shift in neuronavigation of brain tumors: A review, Medical Image Analysis 35 (2017) 403–420. doi:10.1016/j.media.2016.08.007.
URL https://linkinghub.elsevier.com/retrieve/pii/S1361841516301566

[3] W. Penfield, E. Boldrey, Somatic motor and sensory representation in the cerebral cortex of man as studied by electrical stimulation, Brain 60 (4) (1937) 389–443. doi:10.1093/brain/60.4.389.
URL https://academic.oup.com/brain/article-lookup/doi/10.1093/brain/60.4.389

[4] F. F. Jöbsis, Noninvasive, Infrared Monitoring of Cerebral and Myocardial Oxygen Sufficiency and Circulatory Parameters, Science, New Series 198 (4323) (1977) 1264–1267.
URL http://www.jstor.org/stable/1745848

[5] B. Chance, Z. Zhuang, C. UnAh, C. Alter, L. Lipton, Cognition-activated low-frequency modulation of light absorption in human brain., Proceedings of the National Academy of Sciences 90 (8) (1993) 3770–3774. doi:10.1073/pnas.90.8.3770.
URL http://www.pnas.org/cgi/doi/10.1073/pnas.90.8.3770

[6] E. M. C. Hillman, Optical brain imaging in vivo: techniques and applications from animal to man, Journal of Biomedical Optics 12 (5) (2007) 051402. doi:10.1117/1.2789693.
URL http://biomedicaloptics.spiedigitallibrary.org/article.aspx?doi=10.1117/1.2789693

[7] F. Lange, F. Peyrin, B. Montcel, Broadband time-resolved multi-channel functional near-infrared spectroscopy system to monitor in vivo physiological changes of human brain activity, Appl. Opt. 57 (22) (2018) 6417–6429. doi:10.1364/AO.57.006417.
URL http://ao.osa.org/abstract.cfm?URI=ao-57-22-6417

[8] S. Mottin, B. Montcel, H. Guillet de Chatellus, S. Ramstein, Functional white laser imaging to study brain oxygen uncoupling/re-coupling in songbirds, Journal of cerebral blood flow and metabolism : official journal of the International Society of Cerebral Blood Flow and Metabolism 31 (2010) 393–400. doi:10.1038/jcbfm.2010.189.

[9] S. Mottin, B. Montcel, H. Chatelus, S. Ramstein, C. Vignal, N. Mathevon, Corrigendum: Functional white laser imaging to study brain oxygen uncoupling/re-coupling in songbirds, Journal of cerebral blood flow and metabolism : official journal of the International Society of Cerebral Blood Flow and Metabolism 31 (2011) 1170. doi:10.1038/jcbfm.2010.206.

[10] C. Vignal, T. Boumans, B. Montcel, S. Ramstein, M. Verhoye, J. Van Audekerke, N. Mathevon, A. Van Der Linden, S. Mottin, Measuring brain hemodynamic changes in a songbird: responses to hypercapnia measured with functional MRI and near-infrared spectroscopy, Phys Med Biol 53 (2008) 2457–2470.
URL https://hal.archives-ouvertes.fr/hal-00443490

[11] B. Montcel, R. Chabrier, P. Poulet, Time-resolved absorption and haemoglobin concentration difference maps: a method to retrieve depth-related information on cerebral hemodynamics, Optics Express 14 (25) (2006) 12271–12287.
URL https://hal.archives-ouvertes.fr/hal-00443365

[12] S. Mottin, B. Montcel, Birds Brain: Using Picosecond optical tomography to Assess Neural Activity, Optics and photonics news 23 (11) (2012) 40–47.
URL https://hal.archives-ouvertes.fr/hal-01912458

[13] A. Grinvald, E. Lieke, R. D. Frostig, C. D. Gilbert, T. N. Wiesel, Functional architecture of cortex revealed by optical imaging of intrinsic signals, Nature 324 (1986) 361–364. doi:10.1038/324361a0.

[14] R. D. Frostig, E. E. Lieke, D. Y. Ts'o, A. Grinvald, Cortical functional architecture and local coupling between neuronal activity and the microcirculation revealed by in vivo high-resolution optical imaging of intrinsic signals., Proceedings of the National Academy of Sciences 87 (16) (1990) 6082–6086. doi:10.1073/pnas.87.16.6082.
URL http://www.pnas.org/cgi/doi/10.1073/pnas.87.16.6082

[15] A. Grinvald, D. Shoham, A. Shmuel, D. Glaser, I. Vanzetta, E. Shtoyerman, H. Slovin, C. Wijnbergen, R. Hildesheim, A. Arieli, In-vivo Optical Imaging of Cortical Architecture and Dynamics, in: U. Windhorst, H. Johansson (Eds.), Modern Techniques in Neuroscience Research, Springer Berlin Heidelberg, Berlin, Heidelberg, 1999, pp. 893–969. doi:10.1007/978-3-642-58552-4_34.
URL http://link.springer.com/10.1007/978-3-642-58552-4_34

[16] H. D. Lu, G. Chen, J. Cai, A. W. Roe, Intrinsic signal optical imaging of visual brain activity: Tracking of fast cortical dynamics, NeuroImage 148 (2017) 160–168. doi:10.1016/j.neuroimage.2017.01.006.
URL https://linkinghub.elsevier.com/retrieve/pii/S105381191730006X

[17] J. Pichette, A. Laurence, L. Angulo, F. Lesage, A. Bouthillier, D. K. Nguyen, F. Leblond, Intraoperative video-rate hemodynamic response assessment in human cortex using snapshot hyperspectral optical imaging, Neurophotonics 3 (4) (2016) 045003. doi:10.1117/1.NPh.3.4.045003.
URL http://neurophotonics.spiedigitallibrary.org/article.aspx?doi=10.1117/1.NPh.3.4.045003

[18] M. Mori, T. Chiba, A. Nakamizo, R. Kumashiro, M. Murata, T. Akahoshi, M. Tomikawa, Y. Kikkawa, K. Yoshimoto, M. Mizoguchi, T. Sasaki, M. Hashizume, Intraoperative visualization of cerebral oxygenation using hyperspectral image data: a two-dimensional mapping method, International Journal of Computer Assisted Radiology and Surgery 9 (6) (2014) 1059–1072. doi:10.1007/s11548-014-0989-9.
URL http://link.springer.com/10.1007/s11548-014-0989-9

[19] A. Grinvald, C. C. H. Petersen, Imaging the Dynamics of Neocortical Population Activity in Behaving and Freely Moving Mammals, in: M. Canepari, D. Zecevic, O. Bernus (Eds.), Membrane Potential Imaging in the Nervous System and Heart, Springer International Publishing, Cham, 2015, pp. 273–296. doi:10.1007/978-3-319-17641-3_11.
URL https://doi.org/10.1007/978-3-319-17641-3_11

[20] D. Malonek, A. Grinvald, Interactions between electrical activity and cortical microcirculation revealed by imaging spectroscopy: Implications for functional brain mapping 272 (1996) 551–4.

[21] J. Berwick, C. Martin, J. Martindale, M. Jones, D. Johnston, Y. Zheng, P. Redgrave, J. Mayhew, Hemodynamic Response in the Unanesthetized Rat: Intrinsic Optical Imaging and Spectroscopy of the Barrel Cortex, Journal of Cerebral Blood Flow & Metabolism 22 (6) (2002) 670–679. doi:10.1097/00004647-200206000-00005.
URL http://journals.sagepub.com/doi/10.1097/00004647-200206000-00005

[22] A. Steimers, M. Gramer, B. Ebert, M. Füchtemeier, G. Royl, C. Leithner, J. P. Dreier, U. Lindauer, M. Kohl-Bareis, Imaging of cortical haemoglobin concentration with RGB reflectometry, Munich, Germany, 2009, p. 736813. doi:10.1117/12.831583.
URL http://proceedings.spiedigitallibrary.org/proceeding.aspx?doi=10.1117/12.831583

[23] M. Oelschlägel, T. Meyer, H. Wahl, S. B. Sobottka, M. Kirsch, G. Schackert, U. Morgenstern, Evaluation of intraoperative optical imaging analysis methods by phantom and patient measurements, Biomedizinische Technik/Biomedical Engineering 58 (3). doi:10.1515/bmt-2012-0077.
URL https://www.degruyter.com/view/j/bmte.2013.58.issue-3/bmt-2012-0077/bmt-2012-0077.xml

[24] M. B. Bouchard, B. R. Chen, S. A. Burgess, E. M. C. Hillman, Ultra-fast multispectral optical imaging of cortical oxygenation, blood flow, and intracellular calcium dynamics, Optics Express 17 (18) (2009) 15670. doi:10.1364/OE.17.015670.
URL https://www.osapublishing.org/oe/abstract.cfm?uri=oe-17-18-15670

[25] M. Veldsman, T. Cumming, A. Brodtmann, Beyond BOLD: Optimizing functional imaging in stroke populations: Optimizing BOLD Imaging in Stroke, Human Brain Mapping 36 (4) (2015) 1620–1636. doi:10.1002/hbm.22711.
URL http://doi.wiley.com/10.1002/hbm.22711

[26] C. Caredda, L. Mahieu-Williame, R. Sablong, M. Sdika, J. Guyotat, B. Montcel, Real time intraoperative functional brain mapping using a RGB camera, in: J. Q. Brown, T. G. van Leeuwen (Eds.), Clinical and Preclinical Optical Diagnostics II, Vol. 11073, International Society for Optics and Photonics, SPIE, 2019, pp. 17 – 21. doi:10.1117/12.2526992.
URL https://doi.org/10.1117/12.2526992

[27] C. Caredda, L. Mahieu-Williame, R. Sablong, M. Sdika, L. Alston, J. Guyotat, B. Montcel, Intraoperative quantitative functional brain mapping using an RGB camera, Neurophotonics 6 (4) (2019) 1 – 14. doi:10.1117/1.NPh.6.4.045015.
URL https://doi.org/10.1117/1.NPh.6.4.045015

[28] G. Bradski, The OpenCV Library, Dr. Dobb's Journal of Software Tools.

[29] B. Schling, The Boost C++ Libraries, XML Press, 2011.

[30] M. Sdika, L. Alston, D. Rousseau, J. Guyotat, L. Mahieu-Williame, B. Montcel, Repetitive motion compensation for real time intraoperative video processing, Medical Image Analysis 53 (2019) 1 – 10. doi:https://doi.org/10.1016/j.media.2018.12.005.
URL http://www.sciencedirect.com/science/article/pii/S1361841518308752

[31] M. Sdika, L. Alston, L. Mahieu-Williame, J. Guyotat, D. Rousseau, B. Montcel, Robust real time motion compensation for intraoperative video processing during neurosurgery, in: 2016 IEEE 13th

International Symposium on Biomedical Imaging, IEEE, Prague, Czech Republic, 2016, pp. 1046–1049. doi:10.1109/ISBI.2016.7493445.
URL http://ieeexplore.ieee.org/document/7493445/

[32] M. Kohl-Bareis, B. Ebert, J. P. Dreier, C. Leithner, U. Lindauer, G. Royl, Apparatus for measuring blood parameters (11 2012).

[33] Optical absorption of hemoglobin, https://omlc.org/spectra/hemoglobin/.

[34] Q. Fang, D. A. Boas, Monte Carlo simulation of photon migration in 3d turbid media accelerated by graphics processing units, Optics express 17 (22) (2009) 20178–20190.

[35] W. Penny, K. Friston, J. Ashburner, S. Kiebel, T. E. Nichols, Statistical Parametric Mapping: The Analysis of Functional Brain Images, 2007. doi:10.1016/B978-0-12-372560-8.X5000-1.

[36] C. Caredda, L. Mahieu-Williame, R. Sablong, M. Sdika, J. Guyotat, B. Montcel, Pixel-wise modified Beer-Lambert model for intraoperative functional brain mapping, in: J. Q. Brown, T. G. van Leeuwen (Eds.), Clinical and Preclinical Optical Diagnostics II, Vol. 11073, International Society for Optics and Photonics, SPIE, 2019, pp. 148 – 152. doi:10.1117/12.2527045.
URL https://doi.org/10.1117/12.2527045

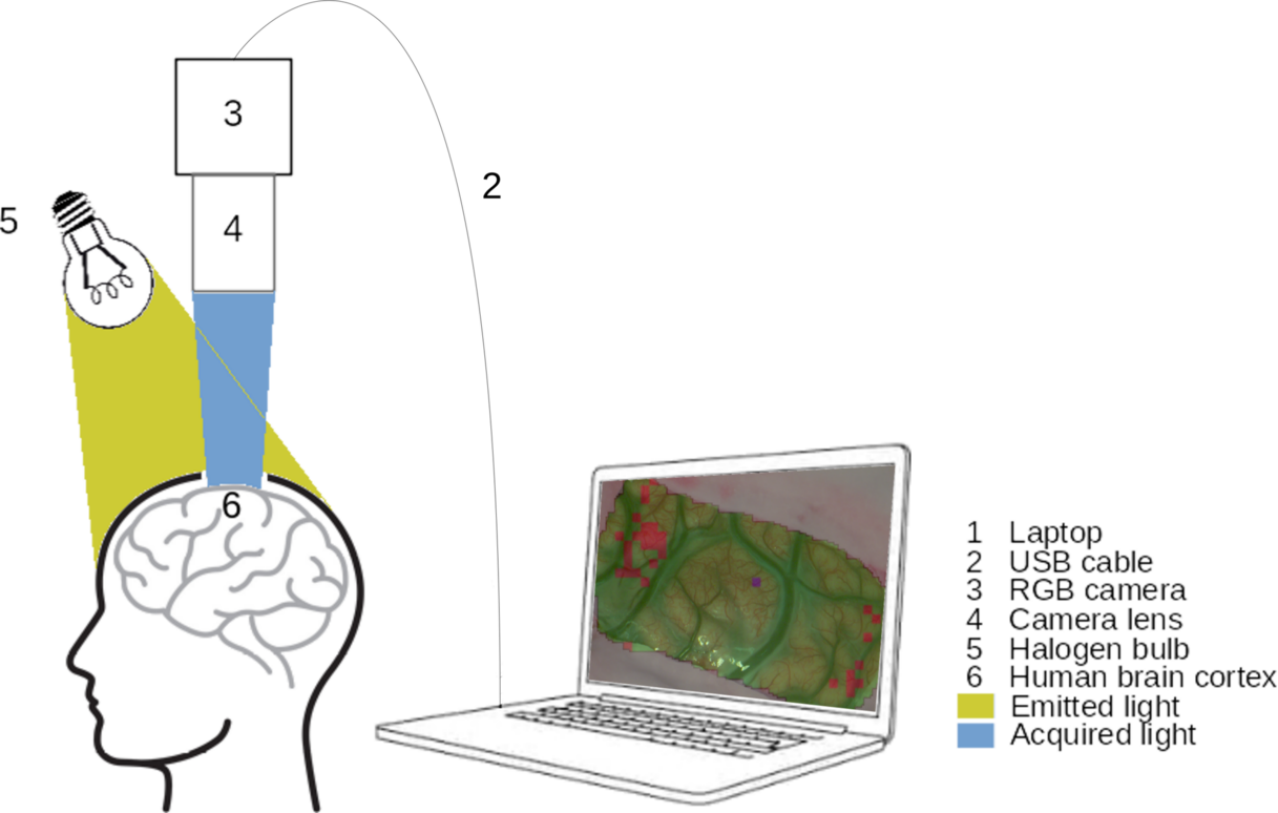
3
4
5
2
6
1 Laptop
2 USB cable
3 RGB camera
4 Camera lens
5 Halogen bulb
6 Human brain cortex
Emitted light
Acquired light